

Possible temperate lakes on Titan



Graham Vixie^{a,*}, Jason W. Barnes^a, Brian Jackson^b, Sébastien Rodriguez^c, Stéphane Le Mouélic^d, Christophe Sotin^e, Shannon MacKenzie^a, Paul Wilson^f

^a University of Idaho, Department of Physics, 875 Perimeter Drive MS0903, Moscow, ID 83844-0903, USA

^b Department of Terrestrial Magnetism, Carnegie Institution of Washington, 5241 Broad Branch Road, NW, Washington, DC 20015-1305, USA

^c Laboratoire AIM, Université Paris Diderot – Paris 7/CNRS/CEA-Saclay, DSM/IRFU/SAP, Gif sur Yvette, France

^d Laboratoire Planétologie et Géodynamique de Nantes LPGN/CNRS UMR6112, Université de Nantes, Nantes, France

^e California Institute of Technology/Jet Propulsion Laboratory, 4800 Oak Grove Drive, Pasadena, CA 91109, USA

^f Energyneering Solutions, 15820 Barclay Drive, Sisters, OR 97759, USA

ARTICLE INFO

Article history:

Received 5 March 2014

Revised 3 May 2015

Accepted 10 May 2015

Available online 19 May 2015

Keywords:

Titan, hydrology

Titan, atmosphere

Titan, surface

Radiative transfer

ABSTRACT

We analyze southern mid-latitude albedo-dark features on Titan observed by *Cassini's* Visual and Infrared Mapping Spectrometer (VIMS). In exploring the nature of these features we consider their morphology, albedo, and specular reflectivity. We suggest that they represent candidates for potential temperate lakes. The presence of lakes at the mid-latitudes would indicate that surface liquid can accumulate and remain stable away from Titan's poles. Candidate lakes were identified by looking for possible shorelines with lacustrine morphology. Then, we applied an atmospheric correction that empirically solved for their surface albedo. Finally, we looked for a specular reflection of the sky in the identified candidates. Using this prescription, we find two candidates that remain as potential temperature lakes. If candidate features do represent temperate lakes on Titan, they have implications for formation mechanisms such as clouds and rainfall or, in low elevation areas, percolation and subsurface flow. Clouds were observed near candidate lake locations on the T66 flyby and this latitude band showed many clouds during southern summer. Our techniques can be applied to areas of Titan that lack RADAR coverage to search for mid- and low-latitude lakes in the future.

© 2015 Elsevier Inc. All rights reserved.

1. Introduction

Titan's atmosphere obscures the surface for the majority of visible-infrared wavelengths at which *Cassini* observes. In the methane windows where surface features are visible, scattering off of atmospheric haze particles can dilute the pure surface signal, reducing contrast and smearing out fine-resolution imaging. Scattering in the atmosphere also leads to ambiguities in the spectrum because the returned signal represents a superposition of atmospheric and surface contributions.

Lorenz (1994) surmised that lakes (as opposed to expansive oceans) may exist across the surface of Titan. The T16 *Cassini* RADAR synthetic aperture radar (SAR) swath over the north pole revealed many lakes, both dry and liquid-filled (Stofan et al., 2007). The first south-polar lake observed on Titan was Ontario Lacus by the Imaging Science Subsystem (ISS) and VIMS (Brown et al., 2008; Turtle et al., 2009; Barnes et al., 2009; Hayes et al., 2010; Cornet et al., 2012a,b). As *Cassini* continues to observe

Titan, we have come to know that filled lakes on Titan are concentrated at the poles (Hayes et al., 2008), while all of the observed deserts and dunes are near the equator (Lorenz et al., 2006; Lorenz and Radebaugh, 2009; Le Gall et al., 2011, 2012; Rodriguez et al., 2014).

Boundary conditions on global circulation imply that volatiles build up at the poles (Tokano, 2009). Mitri et al. (2007) points to methane as being the transient liquid present in lakes. However, Stofan et al. (2007) and Tan et al. (2013) state that liquid methane is thermodynamically stable anywhere on the surface of Titan. Clouds have been seen to concentrate around the 40°S latitude mark (Griffith et al., 2005; Roe et al., 2005; Brown et al., 2010; Rodriguez et al., 2009, 2011; Turtle et al., 2011a) whereas no persistent surface liquids had been previously identified equatorward of 70°S or 53°N latitude. Rainfall has been shown to modify Titan's surface reflectance (Turtle et al., 2011b; Barnes et al., 2013), and recent observations suggest that equatorial lakes may also exist (Griffith et al., 2012).

In this paper, we show and analyze observations from *Cassini* VIMS over the south mid-latitudes during the T66 flyby (*Cassini* Rev125, the spacecraft's 127th revolution around Saturn, January

* Corresponding author.

E-mail address: gvixie@vandals.uidaho.edu (G. Vixie).

28, 2010). We then construct a simple radiative transfer model for use with Titan data and fit for surface albedos. The results of the model are then used to present evidence for two potential lakes near 40°S. Lakes here would show that liquids can accumulate in the temperate regions, even in very localized areas, allowing us to place constraints on Titan's hydrological cycle. This work, however, cannot absolutely determine these features are indeed lakes nor demonstrate their longevity as albedo-dark.

2. Observations

The T66 flyby of Titan on January 28, 2010 at 22:28 UTC was a high-altitude (7487 km at closest approach) pass with ISS as the prime instrument at closest approach and VIMS riding along. There have been relatively few flybys of Titan with higher altitudes at closest approach (e.g. T9 – 10,409 km, T66 – 7487 km, T67 – 7437 km, T72 – 8175 km, T73 – 7921 km, T75 – 10,053 km, T78 – 5821 km, T80 – 29,415 km, and T81 – 31,131 km). Such flybys allow *Cassini* to attain greater coverage but results in coarser spatial resolution; however, the exposure time does not need to be reduced to very low values, which degrades the signal-to-noise ratio.

VIMS performed high (3.7 km/pixel) and moderate (16 km/pixel) spatial sampling centered around Polaznik Macula, a dark feature at 79.6°E, 41.1°S originally named from ISS imaging. Additionally at closest approach, VIMS took one shorter and one longer exposure time cube. The cubes covering the Polaznik Macula area are listed with their characteristics in Table 1 in time order during approach. All of the relevant angles are recorded from as close to closest approach as coverage permits in the south-east portion of Polaznik. As *Cassini* neared closest approach, the values for emission and phase angles showed more variance than incidence angles, which changed more slowly due to Titan's slow rotation.

Fig. 1 shows the global location of Polaznik Macula. The south-eastern portion of Polaznik (located at 81.7°E, 41.4°S) stands out in VIMS, appearing to have a lower measured incident radiation over flux ($\frac{I}{I_0}$) than nearby features. Fig. 2 shows an infrared color composite of the Polaznik Macula area, outlined in red, in contrast to its surroundings. The initial hypothesis is that this south-eastern area, outlined in dark blue in Fig. 2, may represent a lake currently filled with liquid, now named Sionascaig Lacus. No RADAR SAR observations of the Polaznik Macula area currently exist; were such observations to be acquired, they would be of use to help to test the lacustrine hypothesis.

A second area just past the upper right boundary of the darkened area (also outlined in dark blue) shows a similar contrast to the lower right area and is also hypothesized to be a filled lake, now named Urmia Lacus. The other areas outlined in light blue show slightly brighter surface reflectivities and may be candidates for lakes, though they remain unconfirmed. Section 5 discusses the

possibility and implications of these outlined areas being filled lakes.

3. Atmospheric correction and surface albedo retrieval

Approximating a full atmospheric transfer function allows correction of past, present, and future flyby data to reveal surface albedos, that is, the albedo of the surface compensating completely for atmospheric effects. Early classical, numerical radiative transfer models developed for Titan such as Rages and Pollack (1980), Pollack et al. (1980), Podolak et al. (1984), Lockwood et al. (1986), McKay et al. (1989), Griffith et al. (1991) and Rannou et al. (1995) used Voyager and ground-based data analysis. During the two following decades, those teams and others continued to improve their models with a multitude of publications occurring right after *Cassini*'s arrival at Saturn and the Huygens landing. Several approaches were developed, including first-order scattering models (Rodriguez et al., 2006), empirical corrections for atmospheric contribution and surface photometry (Cornet et al., 2012a; Le Mouélic et al., 2012), and a 3D spherical Monte-Carlo model accounting only for haze scattering to probe the vertical distribution of aerosols down to the surface (Vincendon and Langevin, 2010), for example. Each model's results can be compared with ground-based and *Cassini* data to explore unresolved or unknown regions of interest on Titan through the use of creating synthetic spectra or interpreting images, for example. Numerical radiative transfer models are powerful tools for Titan research, but poorly constrained inputs can often lead to very long computation times (i.e., running the model over a large input range, a large number of inputs, or both).

Radiative transfer models can identify the surface albedo and characterize liquid regions with confidence, which have very low albedo in the infrared (Griffith et al., 2012).

We have implemented a partial, analytical, single-scattering atmospheric correction in order to derive surface albedo from measured $\frac{I}{I_0}$ in the VIMS 5 μm spectral region. We fit the model, upgraded from that in Barnes et al. (2009), using a Levenberg-Marquardt least-squares minimization algorithm. We define $\frac{I}{I_0}$ to be the total measured upward intensity divided by the incident solar flux. We make the assumption that contribution from photons scattered multiple times by the atmosphere is negligible – a good approximation at 5 μm (Rodriguez et al., 2006; Brown et al., 2008). The contributions to $\frac{I}{I_0}$ that we do consider are:

- radiation reflected from the surface, wholly unscattered on its trip down through the atmosphere or back up,
- radiation scattered upward by the atmosphere before reaching the surface, and
- radiation scattered by the atmosphere downward into the surface, then reflected back upward by the surface and unscattered on its passage out of the atmosphere.

Table 1

Characteristics of Relevant T66 VIMS Cubes: These cubes from the T66 flyby form the composite image (Fig. 2) in which we outline Sionascaig Lacus and Urmia Lacus. The cubes are listed in order of approach as seen from the best spatial resolution and range columns. All of the relevant angles are recorded from either in Sionascaig Lacus or as close as the cube covers to that area. As *Cassini* flies by at closest approach, the values for emission and phase show more variance than incidence.

VIMS cube	Best spatial sampling (km)	Range (km)	Incidence (°)	Emission (°)	Phase (°)	Exposure time (ms)
CM_1643417608_1	16.5	32,672	45	46	39.5	120
CM_1643416678_1	14.0	27,745	46	41	43	120
CM_1643414307_1	8.24	15,802	48	46	38	120
CM_1643413825_1	7.13	13,616	51	46	38	120
CM_1643413339_1	5.81	11,588	51	44	39	120
CM_1643412870_1	4.82	9881	52	36	41.5	120
CM_1643412398_1	4.00	8530	49	22	50	120
CM_1643411921_1	3.74	7691	50	17.5	59.5	140
CM_1643411254_1	3.82	7637	51	31	82.5	40
CM_1643411453_1	3.66	7509	51	23	74.5	120

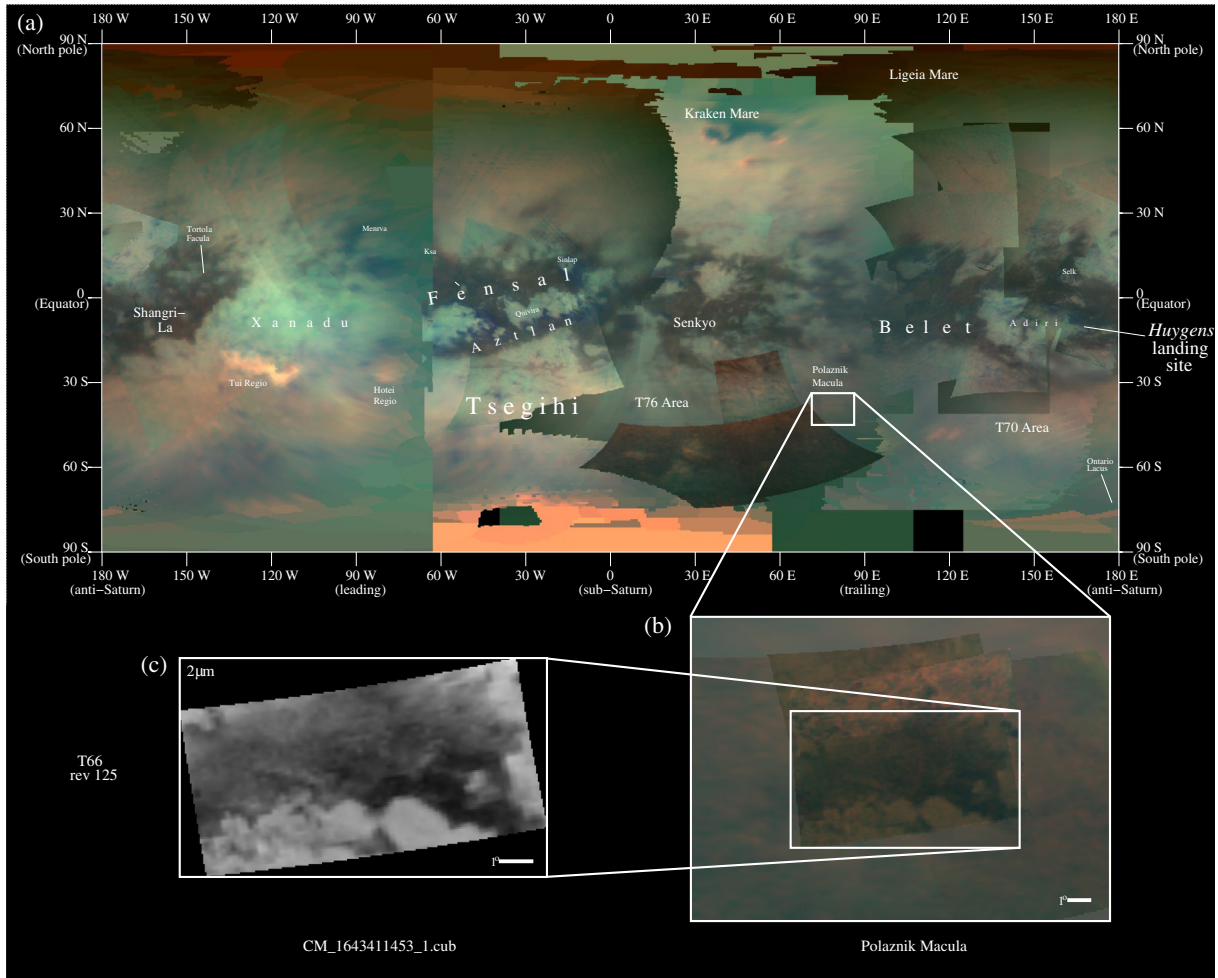


Fig. 1. This cylindrical projected global map is annotated with several points of interest and significant features of Titan's surface. The false color composite (a at top) uses 1.28 μm as blue, 2.00 μm as green, and 4.8–5.2 μm as red. Fewer images were chosen to minimize the number of seams while maximizing global coverage rather than simply using all of the highest resolution cubes available. Polaznik Macula is of particular interest here and the area has been enlarged in subfigures (b) and (c). The first enlarged composite image in subfigure (b), using the same wavelength combination as (a), is part of the T66 (Rev25) flyby of Titan by the *Cassini* spacecraft, built from the cubes listed in Table 1. Another box is drawn around the macula itself and enlarged again to show a single 2 μm image in subfigure (c) from T66, emphasizing the contrast of the features within. (For interpretation of the references to color in this figure legend, the reader is referred to the web version of this article.)

We calculate effective $\frac{I}{F}$ using the following equation:

$$\frac{I}{F} = A\Phi_s(i, e, \varphi)e^{-\tau(\alpha(i)+\alpha(e))} \quad (1)$$

$$+ \frac{\tilde{\omega}_0 p(\hat{\Omega}_0, \hat{\Omega})}{4\pi} \frac{\alpha(e)}{\alpha(i) + \alpha(e)} [1 - e^{-\tau(\alpha(i)+\alpha(e))}] \quad (2)$$

$$+ A \frac{\tilde{\omega}_0}{4\pi} e^{-\tau\alpha(e)} \int_{\alpha'_+} \Phi_s(i, e, \varphi) \frac{\alpha(\theta')}{\alpha(i) - \alpha(\theta')} p(\hat{\Omega}, \hat{\Omega}') [e^{-\tau\alpha(\theta')} - e^{-\tau\alpha(i)}] d\Omega'. \quad (3)$$

A is the surface albedo. $\Phi_s(i, e, \varphi)$ is the average surface phase function in terms of incidence, emission, and phase angles, calculated from each flyby for each of the model's bins. τ is the total atmospheric extinction optical depth (scattering + absorption). $\alpha(i)$ is the incident airmass, $1/\cosine$ of the solar incident angle for the plane parallel case. Otherwise this is the number of normal atmospheres traversed by the signal on the way down. $\alpha(e)$ is the emission airmass, $1/\cosine$ of the solar emission angle for the plane parallel case. Otherwise this is the number of normal atmospheres traversed by the signal on the way out. $\tilde{\omega}_0$ is the average single

scattering albedo of atmosphere. $p(\hat{\Omega}_0, \hat{\Omega})$ is the average haze phase function for scattering from direction $\hat{\Omega}_0$ into $\hat{\Omega}$, defined as above, where each $d\Omega$ represents the solid angle in the direction $\hat{\Omega}$, given by $\cos(\theta)d\phi d\theta$, where θ and ϕ are the zenith and azimuthal angles to be integrated over, respectively.

This model improves on the work done by Rodriguez et al. (2006), Barnes et al. (2009), Le Mouélic et al. (2012) and Sotin et al. (2012) by adding one additional scattering mode.

The objective is to look at the effective $\frac{I}{F}$ in areas of interest over a variety of phase angles on many different flybys to fit a curve for the unknown parameters in our empirical radiative transfer model, specifically the surface albedo, A . We fit our model using VIMS observations at different observing geometries, i , e , and φ , to measure the unknown parameters τ and $\tilde{\omega}_0$, as well as the surface albedo. The average surface phase function is calculated assuming a Lambertian surface while the incident and emission airmasses are calculated based on an “orange rind” atmospheric model from Barnes et al. (2009).

Our empirical approach assumes that the albedos of visually similar areas are constant, and fits for the albedo of each designated feature substrate type. We create masks over surface features on Titan by manually outlining regions that we assume to

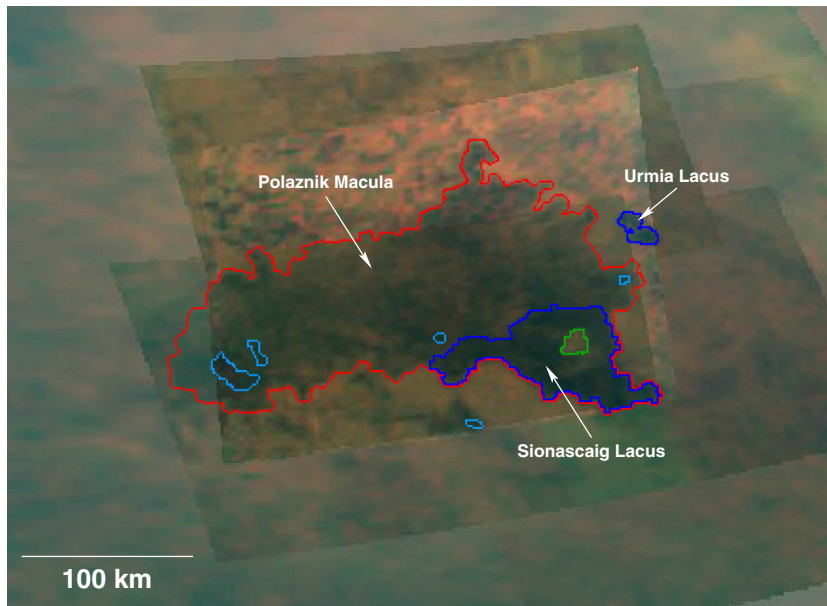


Fig. 2. Polaznik Macula is the large, dark area central to the figure outlined in red. The dark blue encircled areas represent the potential lakes positively identified in the T66 flyby via observed lake-like morphology and surface albedo less than 0.010 (the criterion determined from the well known liquid-filled Kraken Mare and Ligeia Mare). The light blue areas represent lake candidates still under scrutiny, as they have surface albedos less than 0.010 but lack definite lacustrine morphology. The green circle marks an island within Sionascaig Lacus. The contrast gradient for this mosaic also shows the central portion of the image to be darker than its surrounding, most noticeably around the edges where our boundaries are drawn. These darkening effects, however, may or may not be the product of varying contrast gradients between differing spatial resolution images, particularly near seams. (For interpretation of the references to color in this figure legend, the reader is referred to the web version of this article.)

have the same albedos. The masks were made by manually outlining areas of interest in Titan flybys where the region was seen by VIMS. We categorize three different mask types from 595 data cubes in the T38, T64–70, and T72 flybys: bright albedo, which covers equatorially bright regions outlined in Barnes et al. (2007); dune albedo, which correlates to the dark brown areas in Barnes et al. (2007, 2008), Soderblom et al. (2007), Rodriguez et al. (2014); and lake albedo. Although the dune fields are known to not be the darkest albedo, we use this region for masking because VIMS has extensive coverage of these areas.

Fig. 3 shows the raw $\frac{I}{F}$ data points with our best-fit model over plotted. The raw data presented in each plot represent every pixel covered by our masks of each region. The mask coverage in the bright and dunes regions includes a wide range of viewing geometries, allowing for a much more accurate fit of the model. Lake observations have suffered because previously identified lakes exist at high latitudes, meaning VIMS coverage has been at high incidence angles. Each plot shows the large range of $\frac{I}{F}$ for a given incidence and emission angle, which in turn lends a visual measure for the goodness of fit for the model. The reduced χ^2 value for our plots is 4.72, most likely due to our binning assumption, which in turn increases variance. Our reduced χ^2 quantifies the deviation of the model's prediction from the actual values, assuming each actual value pixel within the same substrate has the same surface albedo. The bright and dune regions tend to decrease in $\frac{I}{F}$ with increasing incidence angle but stay somewhat constant with emission; changes in emission affect the dune region slightly more. The emission angle drives an increase in the lake region $\frac{I}{F}$ most noticeably above the 60° mark. There is also a subtle decrease in the $\frac{I}{F}$ at high emission and high incidence angles as pointed out by arrows in Fig. 3c and d. All data points also vary in phase (not shown) which may explain some outliers in the plots. The phase in the best-fit model is the angle between each incidence and emission angle pair for each point, calculated by the model.

The variation in contrast in Fig. 2 is due to the variation in illumination geometry from various observations. By calculating the $\frac{I}{F}$

ratio on either side of these seams, we gain a metric for measuring the uncertainty of our model derived surface albedos. The percent difference in $\frac{I}{F}$ across the seams within Fig. 2 for observed and model derived values places an upper bound on surface albedo uncertainty around $\sim 16\%$. This uncertainty is within tolerance considering our single scattering approximation based model.

The haze phase function, $p(\hat{\Omega}_0, \hat{\Omega})$, is interpolated from a tabular look up based on Tomasko et al.'s (2008) Table 1b, 5166 nm column, and is thus uniform below 80 km altitude. In the process of solving for surface albedo, we fix a minimum number of variables at their best-fit values based on the empirical $\frac{I}{F}$. The $5 \mu\text{m}$ value of $\tilde{\omega}_0$ calculated by our model under many different initial conditions is consistently within up to $\sim 23\%$ of 1.0 (meaning that our empirical fit matches the Tomasko phase function). Thus the surface albedos listed in Table 2 were found using a fixed $\tilde{\omega}_0$ of 1.0, uniform in altitude. Our best fit $5 \mu\text{m}$ value for τ (0.042 ± 0.002) gives a 91% 2-way transmission ($1 - 2\tau$) close to the one estimated by Sotin et al. (2012) using VIMS observations of solar occultations.

We can then apply our model to any VIMS cube, using the best-fit values for τ and $\tilde{\omega}_0$ along with any cube's observed $\frac{I}{F}$, incidence angle, emission angle, and phase angle to solve for the surface albedo of each pixel making the hypothesis that the atmospheric properties have not changed during the interval of observations. Next, we classify features based on observed boundaries and the model's value for each surface feature type (i.e., bright, dune, or lake). We use this method on the T66 flyby, specifically the area shown in Fig. 2, to classify our candidate lake features.

4. Interpretation

4.1. Sionascaig and Urmia

We explore three lines of inquiry to evaluate the lake hypothesis for Sionascaig Lacus and Urmia Lacus: morphology, surface albedo, and specular reflection.

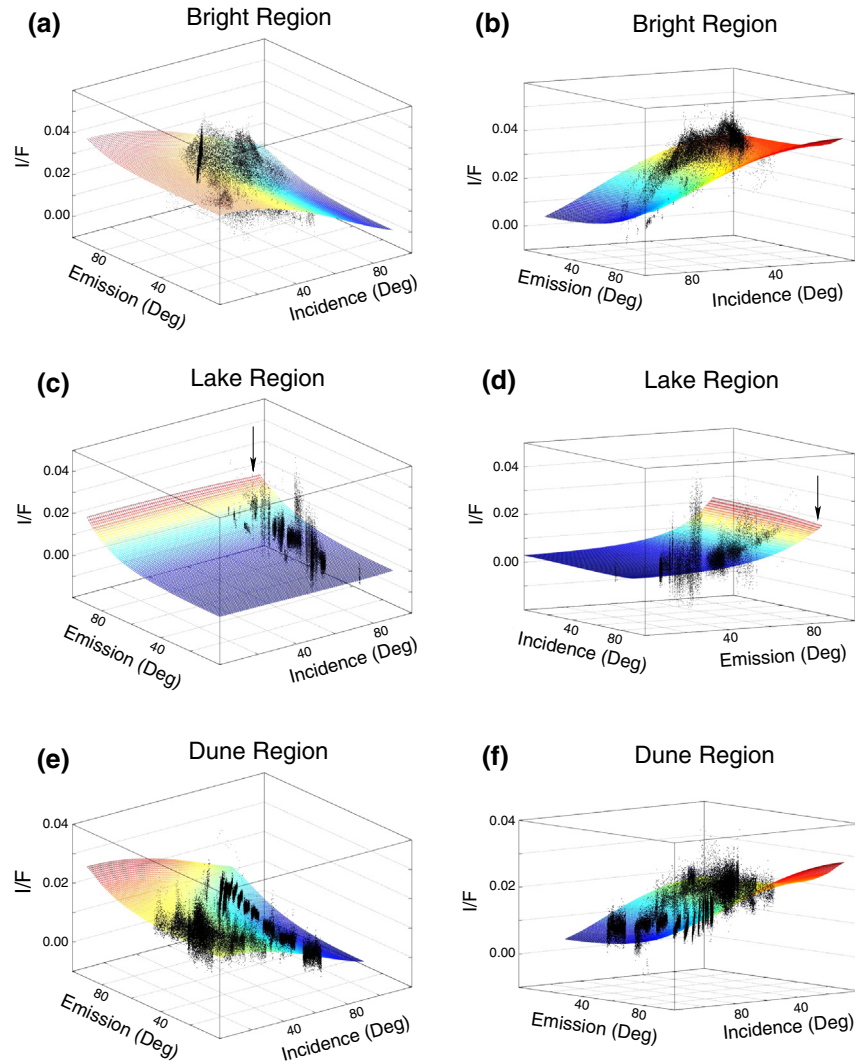


Fig. 3. The six subfigures above show our model plotted along with the raw data for the areas covered by our masks from the VIMS dataset with $\frac{I}{F}$ versus incidence and emission angles. The phase values for the model are calculated to be the real phase values for each point. Each row presents different views of the same 3D plot. (a) and (b) represent the equatorial bright regions for which *Cassini* has a wide range of viewing geometries. This inclusive coverage allows for a more comprehensive model fit in the bright region. Parts (c) and (d) show the lake region. VIMS coverage of lake areas is somewhat limited in terms of viewing geometries as most of the raw data is at high incidence. The arrow indicates a subtle decrease in $\frac{I}{F}$ at high incidence. (e) and (f) quantitatively describe the dunes region which also has a very wide range of viewing geometries in VIMS allowing for a reasonable fit.

Table 2

The free parameters being best-fit by the model run at $5 \mu\text{m}$ along with their results and error where available. Each region entry represents a surface albedo value for the respective substrate. The errors for the bright and dune regions are formal errors that come out of the fit, comprising random errors only. Variation in contrast in observations is due to the variation in illumination geometry from various observations. The percent difference in $\frac{I}{F}$ across the seams within Fig. 2 for observed and model derived values places an upper bound on surface albedo uncertainty around $\sim 16\%$. This uncertainty is within tolerance considering our single scattering approximation based model.

Parameters	Model result (error)
τ	0.0428 (± 0.002)
ω_0	1.0 (fixed)
Bright region	0.0322 (± 0.0005)
Lake region	0.01
Dune region	0.0158 (± 0.0005)

4.1.1. Morphology

The morphology of a large surface feature can be judged to be lacustrine or non-lacustrine by comparing it to other known and verified lakes on Titan, such as Ontario Lacus (Barnes et al., 2009; Wall et al., 2010; Cornet et al., 2012a). The boundary of the bright

dark disparity around each candidate feature is continuous, lobate, and relatively similar to previously identified VIMS, RADAR, and ISS lakes. Comparisons to Ontario Lacus can be made looking at Figs. 3 and 6 from Barnes et al. (2009), Fig. 1 from Wall et al. (2010), and Figs. 1 and 4 from Cornet et al. (2012a). The boundaries of the features outlined in dark blue in Fig. 2 are consistent with these comparisons for shoreline in the VIMS data.

We took $\frac{I}{F}$ transects across Ontario Lacus, Punga Mare, Kivu Lacus, and Sionascaig Lacus to further identify boundaries and compare Titan lake behavior. Fig. 4 compares these 4 features by measuring the $\frac{I}{F}$ drop across a line perpendicular to the perceived shorelines stretching across to each adjacent shore in the 1.3, 2, and $5 \mu\text{m}$ wavelengths. Here we see Sionascaig matches quite closely to the other lakes in percentage $\frac{I}{F}$ drop, having a 12% drop at $1.3 \mu\text{m}$, 33% at $2 \mu\text{m}$, and reaching an 80% decrease across the transect at $5 \mu\text{m}$. For this comparison, Sionascaig's behavior is consistent with other lakes in VIMS.

An aeolian sand sheet may also exhibit similar morphology when filling in a depression. However, the bright feature within dark Sionascaig does not exhibit typical aeolian morphology, e.g.

a trailing feature on the lee side of an obstacle as seen in [Lorenz et al. \(2006\)](#) and [Radebaugh et al. \(2008\)](#). While the VIMS coverage cannot absolutely distinguish lacustrine from aeolian morphology, especially at *Cassini* spatial resolutions, we think an aeolian sand sheet is unlikely ([Radebaugh et al., 2008](#)).

The substrate dichotomy between dark and non-dark is similar to VIMS observations of Kraken Mare and Ligeia Mare as well as other northern lakes as seen in Figs. 4, 7, and 10 from [Sotin et al. \(2012\)](#). The lobate boundaries are akin to VIMS 5 μm observations of those north polar lakes that do not exhibit evaporite around their shorelines seen in Figs. 1 and 2D, F of [Barnes et al. \(2011\)](#). Unfortunately, no future RADAR flybys are planned for the Polaznik Macula area in the Solstice mission, so a greater spatial sampling analysis of morphology here is unlikely. If such coverage existed, we may look for channelized or erosional features to better distinguish the morphologic type.

4.1.2. Albedo

Liquid hydrocarbon surfaces have a very low albedo in the infrared as liquid methane and ethane are strong absorbers in the 5 μm wavelength window ([Clark et al., 2010](#)). The spectra are too noisy for compositional analysis, but are sufficient to extract

albedos at one wavelength—enough to be diagnostic for the presence of liquids. The surface albedo can be read off of an empirically atmospherically corrected map generated by our single-scattering model to compare the albedo to that for known bodies of liquid. The model, as described in the previous section, reports surface albedos within the dark blue areas of [Fig. 2](#) of 0.0070–0.0081 at 5 μm —darker than the darkest areas within the dunes. Specifically, the surface albedo of Sionascaig Lacus is 0.0070 and Urmia Lacus is 0.0081. These values are consistent with those measured albedos for Kraken Mare (0.0114) and Ligeia Mare (0.0050–0.0089) by our model. These values for Kraken Mare and Ligeia Mare are lower than described in [Sotin et al. \(2012\)](#) but remain consistent because the additional scattering modes accounted for in our model lower the albedo by subtracting the contributions from haze scattering. Our value for lake albedo is also lower but within the error bars of [Griffith et al.'s \(2012\)](#) 5 μm lake albedo of 0.02 ± 0.01 . The central area in Polaznik Macula, northwest of Sionascaig Lacus, has a 5 μm albedo of 0.0150, similar to that of the dunes but lower than the dune albedo for 1.08 μm of 0.03–0.08 in [Griffith et al. \(2012\)](#), and lower still than the ISS solid surface dark albedo of 0.05 from [McCord et al. \(2008\)](#). The bright region surrounding Polaznik Macula has a 5 μm surface albedo of

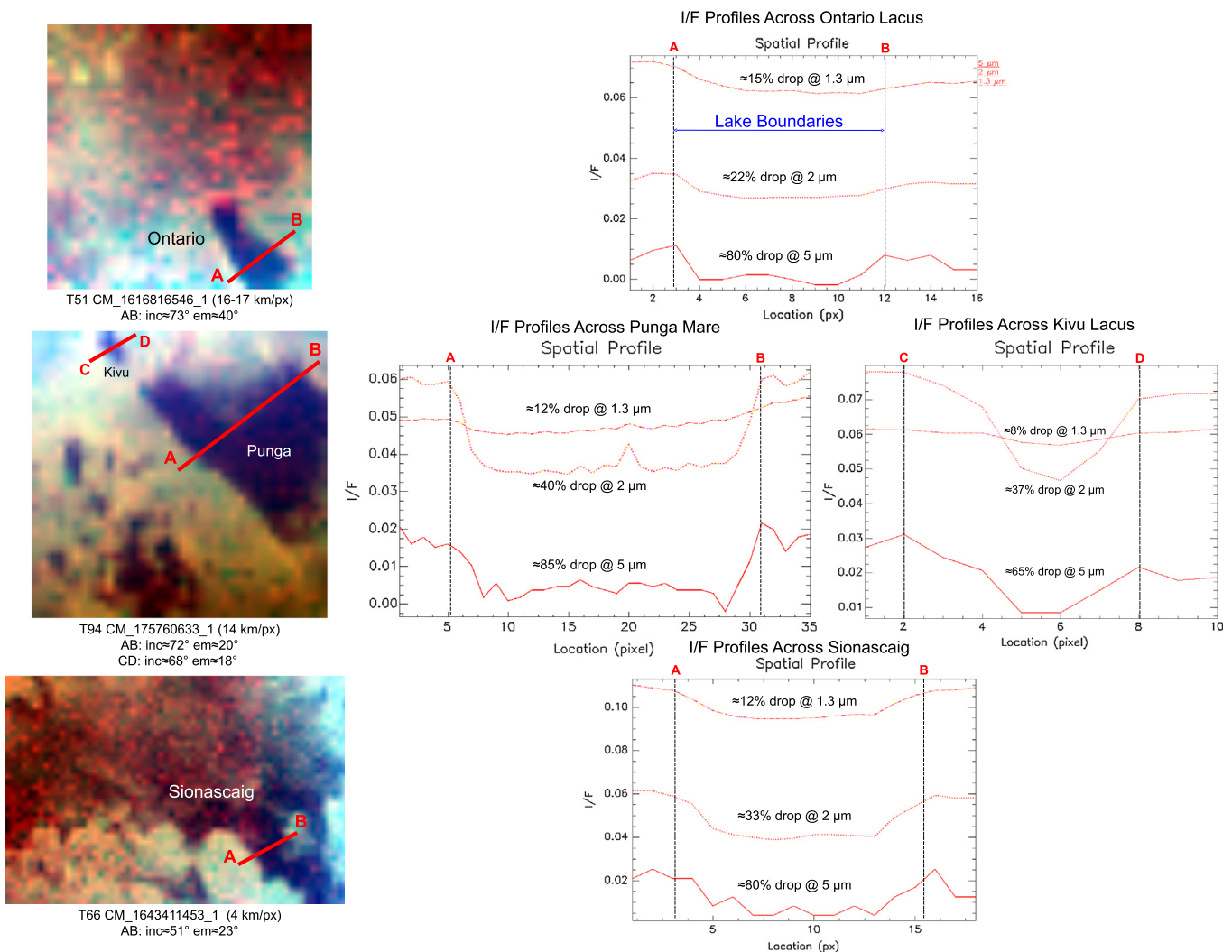


Fig. 4. We take transects across Ontario Lacus (top), Punga Mare and Kivu Lacus (middle), and Sionascaig Lacus (bottom) to measure and compare the drop in I/F in the 1.3, 2, and 5 μm wavelength windows. Each VIMS data cube for the transects was chosen based on optimal spatial resolution. The vertical bars within each plot show the perceived shoreline of each feature. The drop within these boundary bars shows the drop in I/F for each lake as a percentage compared to the neighboring substrate. The percentage drops in I/F across all wavelengths show concurring results between the features. The morphological behavior of Sionascaig Lacus is consistent with known lakes in VIMS coverage.

0.0298. Fig. 5 shows the areas of Polaznik Macula from T66, including Sionascaig Lacus and Urmia Lacus, labeled by their albedos at $5 \mu\text{m}$.

4.1.3. Specular reflection

Our final test to evaluate whether these features are lakes is the observation of a specular reflection. Specifically, we are looking for illumination of the lake by the sky and not by the Sun (Fig. 6). The albedo, in this case, of the lake in question is a measure of the specular reflectivity. For this, we treat the surface when considering the lake region only as specular, instead of Lambertian, obeying the reflectance curve from Soderblom et al. (2012). A specular reflection should produce a higher $\frac{I}{F}$ value than the non-specular surface albedo expected for a liquid feature on Titan. Equation term (3) accounts for the contribution of such a specular reflection from the sky.

The $\frac{I}{F}$ should increase as VIMS views Polaznik Macula from increasing emission angles according to calculations by Soderblom et al. (2012). This increase can be seen when comparing model $\frac{I}{F}$ predictions with and without Equation part (3) in Fig. 7. From this figure, the difference in $\frac{I}{F}$ is most apparent when the emission angle exceeds 60° . Only two of the observations that we have of Polaznik Macula were acquired with emission angles in this range, and unfortunately, these observations are coarse-resolution (Table 1).

If lake candidates indeed exhibit this specular reflection, then the model should report a specular reflectivity of 1. However, in our analysis, the model reports a reflectivity of 0.44 ± 0.13 for Kraken Mare and Ligeia Mare at $5 \mu\text{m}$, leaving the interpretation somewhat ambiguous even in the case of these large seas. Since our model returns a specular reflectivity below 1, our specular reflection test is inconsistent with both a lake interpretation and that of a solid surface at Kraken and Ligeia. Since we have already seen specular reflections of the Sun in Kraken Mare (Stephan et al., 2010), our results are most likely due to limitations with our approach. For example, the total illumination at $5 \mu\text{m}$ may be too low to retrieve a meaningful result.

Present data for Polaznik Macula are as yet insufficient for such a test as views of this area in flybys other than T66 are at a global

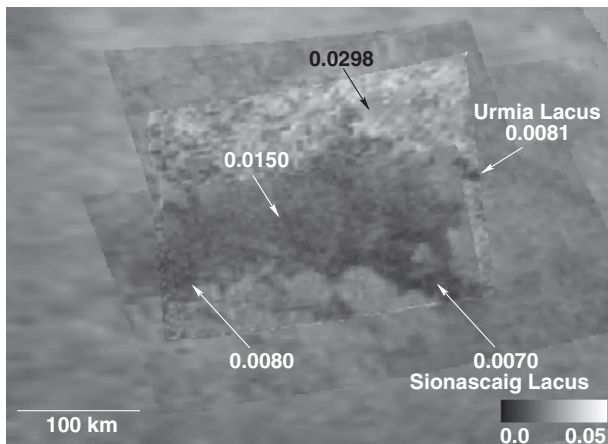


Fig. 5. This figure shows the surface albedos of the different regions considered in this paper. Our model was run on this composite cube from T66 to empirically solve for the surface albedos, fixing the other free parameters of our model, previously determined over test regions (τ and $\hat{\omega}_0$). The northern bright region has a value of 0.0298 ± 0.0005 . The central area of Polaznik Macula has a surface albedo similar to dunes at 0.0150 ± 0.0005 . The two lake areas as well as an area in the west showing no lacustrine morphology all show low surface albedo values similar to Ligeia Mare and Kraken Mare between 0.0070 and 0.0081 . The area in the west could plausibly get its low albedo from wet ground.



Fig. 6. This photograph, taken in flight overland east of Hudson Bay, QC, CAN, shows specular reflections of the sky in several lakes. The dark areas are land; the bright areas are the lakes. This is the kind of specular reflection that we are looking for in Titan's lakes, rather than a direct reflection of the Sun on the liquid as in Stephan et al. (2010).

scale. Working in the $2 \mu\text{m}$ window or a flyby over the Polaznik Macula area where the temperate lakes are near the terminator would provide more atmospheric illumination and could potentially disambiguate these results. However, programming the model to correct the $2 \mu\text{m}$ window is beyond the scope of this paper, and as such, we leave it for future work.

4.2. Other candidates

Finding two potential lakes in the mid-southern-latitudes inspires a search for more lakes that may exist in this temperate latitude band. We surveyed the mid-southern-latitudes for lacustrine morphology and low albedo surface features across Cassini flybys Ta through T72 (the Prime mission through Equinox) and found 10 other candidates. As coverage is at a coarser resolution in the mid-latitudes than at the equator and poles, candidates spanning more than a single pixel are rare.

Seven of the 10 candidates are distinct temperate dark surface features exhibiting possible lacustrine morphology with our model. Evaluating these features we find that the measured surface albedo is higher than what is expected for lake (black arrows in Fig. 8) in each case. The features from T70 are located near 142°E , 42°S while the features from T76 are located at 12°E , 36°S . The remaining two candidate features can be found in T58 and are located near 27°E , 44°S and 59°E , 46°S . A very plausible explanation could simply be that the sampling is too coarse and that the potential lake feature only exists in a few pixels or is even smaller than one pixel. In this case, the average $\frac{I}{F}$ as calibrated from Cassini for each pixel may be higher than that for a potential lake endmember. That is to say, at lower resolution there may be a geographic mixing between lake and surface albedo, resulting in a higher averaged albedo. Confirmation of pixel-scale lakes with VIMS is outside the scope of this study, but may be possible in the future by comparison with RADAR coverage, for example.

The other 3 cases having low albedo exhibit no morphology that would suggest liquid surface features (white arrows in Fig. 8). In this case, the ground may be covered by some low albedo spectral element, may be damp, or the sampling resolution may be too coarse. Turtle et al. (2011b) shows an example of transient liquid darkening the surface after a precipitation event. If the low albedo feature is present in several flybys, then an explanation may be

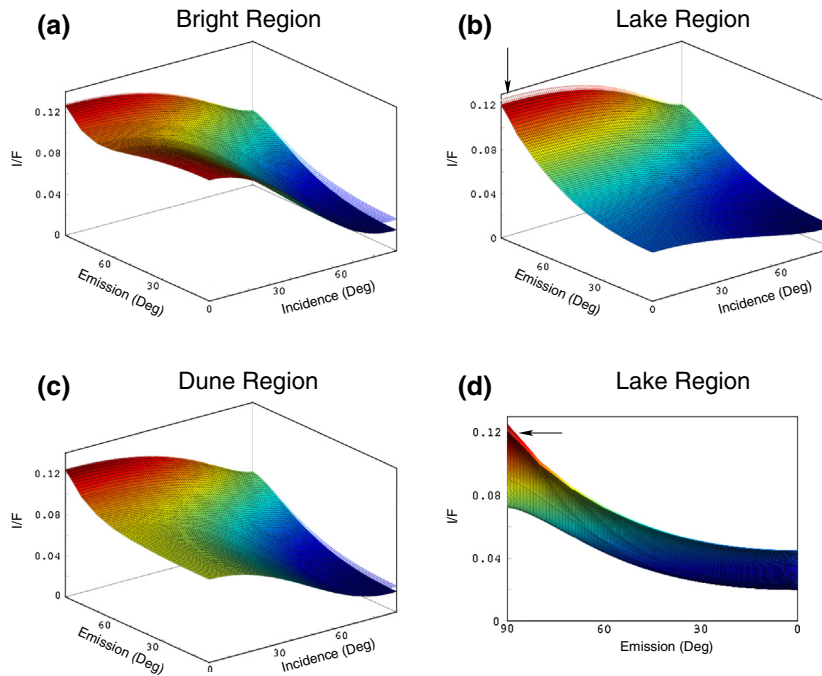


Fig. 7. The solid color surface plot in each subfigure represents our model's prediction of I/F as a function of the incidence and emission angles with only equation terms (1) and (2). The clear mesh plots in each subfigure represent our model with the addition of equation term (3), the sky illumination of the surface. The addition of this final term results in an increased brightness in each terrain type. Plots (a) and (c) show little change in surface albedo except at high incidence and low emission where there is much sky brightening. Plot (b) shows an incidence-independent increase in surface albedo at higher emission pointed to by the arrow. Plot (d) reveals that the lake surface albedo change is most noticeable as emission exceeds 60° , also shown with an arrow. This increase is indicative of a specular reflection of the sky as seen in Fig. 6, but the effect is very subtle at $5 \mu\text{m}$. (For interpretation of the references to color in this figure legend, the reader is referred to the web version of this article.)

similar to the tropical lake proposed in Griffith et al. (2012) and would require further analysis and comparison.

The Griffith et al. (2012) observation of possible tropical lakes provides a good test for our analysis approach. Fig. 9 shows two subfigures of VIMS data cube CM_1567239055_1 from Griffith et al. (2012), shown side by side with other depictions of the same data cube at the same wavelengths. The comparison uses a different contrast stretch in order to better define the morphology of surface features present as per our first test. As the stretch becomes more moderate between Fig. 9b and c, the “dark oval” (Griffith et al., 2012) area becomes less distinct. The abatement of the “dark oval” is more apparent at $2 \mu\text{m}$ (as seen in the comparison of Fig. 9e and f) than at $1.3 \mu\text{m}$. Fig. 10 shows the area in the $5 \mu\text{m}$ wavelength after correction by our model using VIMS data taken from the T35 flyby of Titan; the $5 \mu\text{m}$ data were not used by Griffith et al. (2012). Running our atmospheric correction on the lacustrine candidate area described in Griffith et al. (2012) yields a surface albedo value of 0.0090 on the single darkest pixel in the area, which is consistent with the rest of Titan's lakes. However, the values of the surface albedo in the rest of the “dark oval” area are much higher, ranging from 0.0107 to 0.0167 with an average near 0.0137, which more closely matches the dune region surface albedo. This surface feature also does not exhibit any lacustrine morphology: lack of a distinct shoreline boundary when viewed at $5 \mu\text{m}$ is similar to the areas pointed to by white arrows in Fig. 8.

We caution, though, that we are not able to rule out the presence of surface liquid in the “dark oval” in the Griffith et al. (2012) with our methodology. We note that this candidate does not possess our first or second characteristics. Hence, we would not yet consider the “dark oval” to be a lake with present data. In particular, lacustrine interdunes of the sort sometimes seen within longitudinal sand seas on Earth would not be resolved by current VIMS data and thus cannot be ruled out.

5. Discussion

While we cannot determine the longevity of these candidate temperate lakes without repeat imaging, we can make estimates and comment on the sources, impact, and implications their presence at midlatitudes on Titan's global climatology. In the T66 flyby, which we used to identify the lake candidates, clouds are visible nearby to the southeast and southwest of Polaznik Macula, on the order of $\sim 100 \text{ km}$ away. Throughout Titan's cloud history, clouds are both predicted and observed in southern mid-latitudes during summer, some even specifically around 40°S (Roe et al., 2005; Rodriguez et al., 2009, 2011; Brown et al., 2010). Some clouds have recently been observed around 40°N as well after equinox (Rodriguez et al., 2011; Turtle et al., 2011a). The presence of clouds around Polaznik Macula (41.1°S) suggests at least the possibility that the area could be either a source or a sink for the moisture in the 40°S clouds.

While only the features outlined in blue in Fig. 2 are potentially filled with liquid, the areas outlined in light blue are dark enough to suggest wetting. Specifically the light blue area in the western-most area of Polaznik Macula may be an analog to a muddy or marsh-like feature having a surface albedo of 0.0080, though there is no morphological evidence to support the claim. Barnes et al. (2009) saw similar dark deposits associated with Ontario Lacus, and suggested that they were mudflats. The other light blue areas, though of low albedo, span too few pixels from which to conclude anything definitively.

Mastrogiuseppe et al. (2014) recently showed the average depth of Ligeia Mare to be $\sim 160 \text{ m}$ with a surface area of $120,000 \text{ km}^2$. The surface area of Sionascaig Lacus can be estimated from Fig. 2 to be on the order of $\sim 5000 \text{ km}^2$. The average depth, $d = 0.001 \times \sqrt{\text{area}}$ (Lorenz et al., 2008), would be on the order of 70 m . However, since the altimetry track from Mastrogiuseppe et al. (2014) yields a much shallower 160 m average depth for

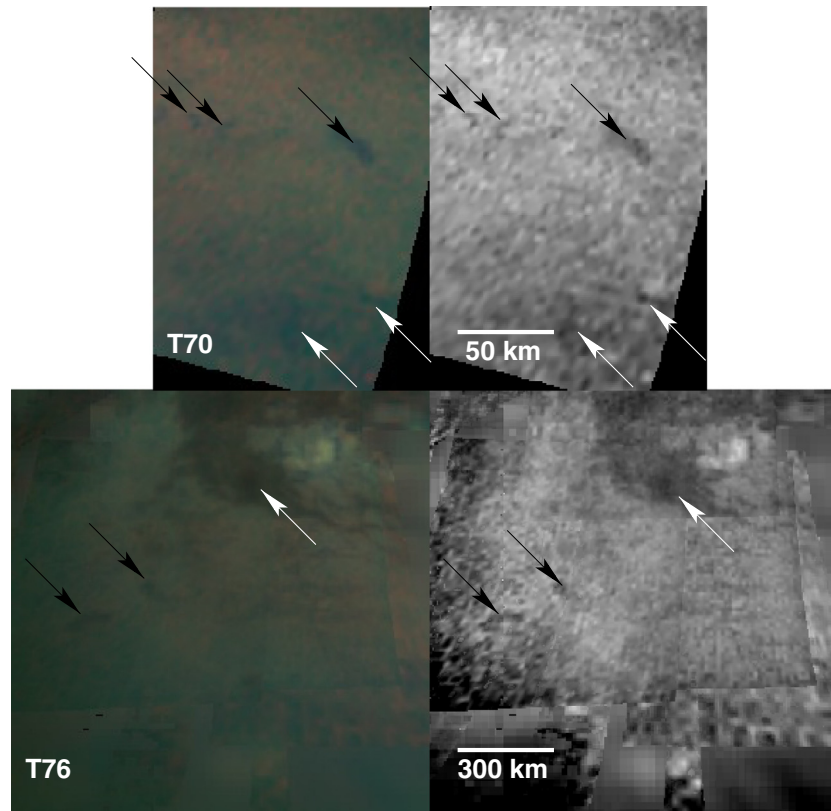


Fig. 8. Two sets of images here from T70 and T76 show our 3-color mosaic outlined in Fig. 1 on the left and the same area in the 5 μm window on the right. Surface features may exhibit lacustrine morphology but have an albedo that is too high, possibly due to coarse sampling resolution. The black arrows here point to surface features whose morphology is suggestive of a shoreline and small, enclosed lake but upon atmospheric correction yield a surface albedo similar to dunes and dark albedo lowlands. White arrows point to dark surface regions that have low albedo consistent with Kraken and Ligeia Mare but give no evidence of shoreline or other lacustrine morphologies. The albedo maps are not shown as the area coverage per pixel for the lake candidates is sufficiently small to not yield meaningful values. (For interpretation of the references to color in this figure legend, the reader is referred to the web version of this article.)

Ligeia Mare, we may also put forth that Sionascaig have an average depth of 40–70 m.

Alternatively, if the slope of Sionascaig's lakebed is similar to the slope of Ontario Lacus (Hayes et al., 2010, 2011) and extends all the way into the feature, then Sionascaig Lacus would have a volume of 920 km^3 with a max depth of 390 m for a slope of 2.7×10^{-3} and 170 km^3 with a max depth of 70 m for a slope of 5×10^{-4} , for a linearly increasing depth. We prefer a more shallow slope with a lesser maximum depth. We argue that this is the case due to similarity between Sionascaig Lacus and Ontario Lacus with analogy to the shallow slopes seen in Google satellite images of San Francisco Bay as the water's opacity does not obscure the ground for the preponderance of the bay (visual analog only). An alternative to shallow slopes may be that the relatively brighter albedo artifacts seen by VIMS within Sionascaig's boundary (Fig. 2) are suspended particles in the liquid.

We then use the smaller volume estimate for Sionascaig Lacus and 453.4 kg/m^3 for the density of liquid methane to estimate the total methane mass to be $7.8 \times 10^{13} \text{ kg}$. Griffith et al. (2005) estimates the total cloud mass for the area bounded by 37°S to 40°S and 0°W to 200°W to be on the order of 10^{10} – 10^{14} kg , with varying conditions. Sionascaig Lacus could then either be controlling cloud formation in this region or a result of cloud activity here.

A possible transport-process for lake liquids on Titan, in addition to rainfall, is percolation or subsurface flow in low-elevation terrain and/or from a high alkanifer (Hayes et al., 2008; Cornet et al., 2012a). The alkanifer hypothesis is also supported by Sotin et al. (2012).

Lorenz et al. (2013) provides a global topographic map of Titan that extrapolates known elevations into areas not yet observed by RADAR. This paper places Sionascaig Lacus in a relative topographic low: around -500 m according to Lorenz et al. (2013), Fig. 3. This interpolated elevation, however, is 700–1000 km from the nearest RADAR reference swath.

Although filled lakes absorb heavily in all of VIMS, ISS, and RADAR wavelengths, the average topography of a lake area can be extrapolated through correlation of RADAR Digital Terrain Models (DTMs). Hayes et al. (2013) find that lake levels are similar in elevation over regional distances in the vicinity of Titan's Mare, supporting an alkanifer hypothesis for this reason. We can also determine relative topography by comparison of RADAR imagery to VIMS or ISS data. This method is accurate for regions closer to existing RADAR coverage. We could more accurately determine the relative elevation of the Sionascaig Lacus area with a RADAR pass over Polaznik Macula by looking at the surrounding altimetry and identifying any channels nearby to suggest drainage. In addition to altimetry, SAR coverage of the area could be a strong complement to the VIMS coverage in the morphological identification of these temperate lacustrine features.

6. Conclusion

Sionascaig Lacus and Urmia Lacus are two candidate lakes within the temperate latitudes of Titan. Both surface features are resolved, appear dark, continuous, and lobate (lacustrine morphology) in VIMS, and our best-fit model places their surface albedos at

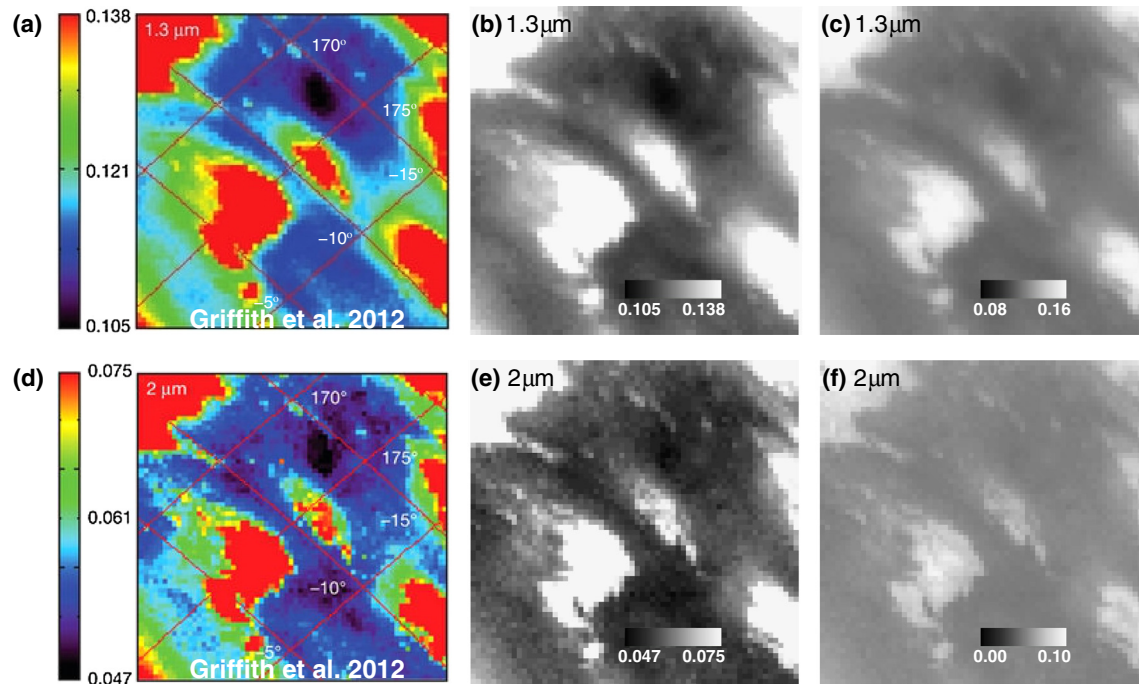


Fig. 9. This figure shows the area of interest from Griffith et al. (2012) in varying contrasts. The two strips above show VIMS cube CM_1567239055_1 from the T35 flyby at 1.3 (Top, a, b, c) and 2.0 (Bottom, d, e, f) microns. Parts (a) and (d) show modified versions of subfigures (a) and (d) from Griffith et al. (2012), Fig. 2. Parts (a)–(c) all display the 1.3 μm channel with part (c) having different contrast limits. Part (b) shows the area at the same contrast stretch as part (a) but without colorization. Many features are saturated in this stretch, so part (c) shows the area with a more moderate stretch. The “dark oval” feature from Griffith et al. (2012) noticeably abates as the rest of the surface features within CM_1567239055_1 become more defined. For further comparison, parts (d)–(f) show the 2.01 μm channel with part (f) differing in contrast. Part (e) again shows the same stretch as part (d) but without colorization. Part (f) has a more moderate stretch and shows the abatement of the “dark oval” to a slightly darker, featureless area. (For interpretation of the references to color in this figure legend, the reader is referred to the web version of this article.)

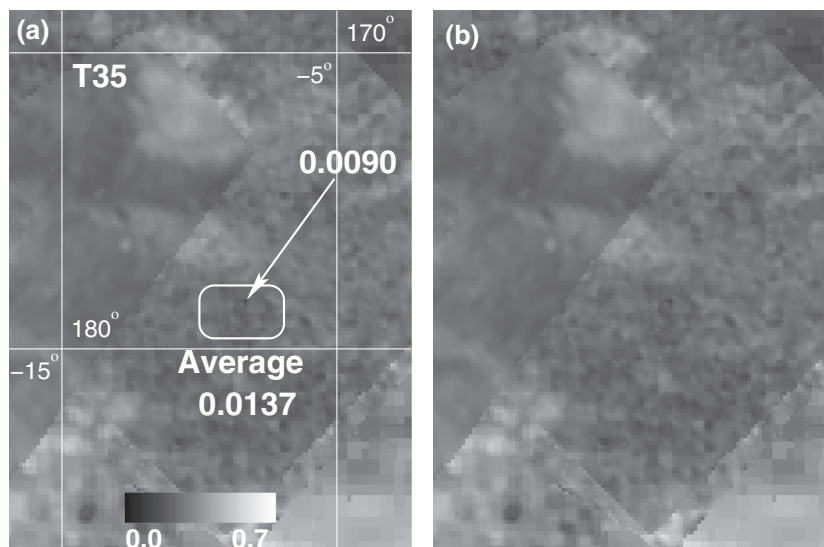


Fig. 10. The figures above show the area around 14°S 173°W, designated in Griffith et al. (2012) as “the dark oval”, at 5 μm as processed by our model. The single darkest pixel in this area has an albedo of 0.0090 and is consistent with lacustrine albedo. However, the average albedo of the area is 0.0137 (from a range of 0.0107 to 0.0167), which is a closer match to dune albedo. There is no well-defined lacustrine morphology when viewed in this area at 5 μm .

0.0070 and 0.0081, respectively, similar to confirmed seas such as Kraken Mare and Ligeia Mare. Therefore, we conclude that these candidates are in fact probably temperate lakes on Titan. Our single-scattering model numerically reports best-fit values for surface albedo, allowing for identification of lakes on Titan lacking RADAR coverage. Unfortunately, we cannot rule out these features being transient.

The majority of the known lakes and seas on Titan are located near the poles. Lakes have been suggested in the tropical zone by Griffith et al. (2012), but that candidate does not meet the criteria applied in our survey. Clouds have been recorded accumulating in the southern mid-latitudes (Griffith et al., 2005; Roe et al., 2005; Brown et al., 2010; Rodriguez et al., 2009, 2011; Turtle et al., 2011a) and areas near 20–30°S latitude have been darkened by

rainfall but later brightened after evaporation (Turtle et al., 2011b; Barnes et al., 2013). Stable temperate lakes would affect total rainfall, liquid accumulation, evaporation rates, and infiltration. Topographic lows may also allow percolation from subsurface reservoirs (Hayes et al., 2008; Cornet et al., 2012a). Our interpretations of Titan's hydrologic cycle are constrained further with the inclusion of probable temperate lakes such as Sionascaig Lacus and Urmia Lacus. With additional VIMS and RADAR coverage, Sionascaig Lacus would make a great candidate for future studies regarding lake filling, evaporation rates, and stability.

The existence of potential lakes outside of the polar areas suggests that the mid-latitudes would be an area of interest for several instruments on *Cassini*. Although VIMS has complete global coverage of Titan, the majority of the mid-latitudes have only been imaged at a very coarse resolution with the one exception being T66, studied here. The mid-latitudes look “bland” and, when combined with coarse sampling resolution, smeared, and cause lacustrine candidates to often span less than a single pixel. As the Solstice tour continues, the improvement of the survey of mid-latitudes will be interesting for the discovery of new lacustrine candidates and for the monitoring of the potential shoreline evolution of Sionascaig Lacus and Urmia Lacus. The cross referencing of areas, if coverage exists, between VIMS, ISS, and RADAR could help to disambiguate the nature of these surface features.

Acknowledgment

The author acknowledges funding by Grant #NNX09AP34G to JWB from the NASA Outer Planets Research Program.

References

- Barnes, J.W. et al., 2007. Global-scale surface spectral variations on Titan seen from Cassini/VIMS. *Icarus* 186, 242–258.
- Barnes, J.W. et al., 2008. Spectroscopy, morphometry, and photoclinometry of Titan's dune fields from Cassini/VIMS. *Icarus* 195, 400–414.
- Barnes, J.W. et al., 2009. Shoreline features of Titan's Ontario Lacus from Cassini/VIMS observations. *Icarus* 201, 217–225.
- Barnes, J.W. et al., 2011. Organic sedimentary deposits in Titan's dry lakebeds: Probable evaporite. *Icarus* 216, 136–140.
- Barnes, J.W. et al., 2013. Precipitation-induced surface brightenings seen on Titan by Cassini VIMS and ISS. *Planet. Sci.* 2.
- Brown, R.H. et al., 2008. The identification of liquid ethane in Titan's Ontario Lacus. *Nature* 454, 607–610.
- Brown, M.E., Roberts, J.E., Schaller, E.L., 2010. Clouds on Titan during the Cassini prime mission: A complete analysis of the VIMS data. *Icarus* 205, 571–580.
- Clark, R.N. et al., 2010. Detection and mapping of hydrocarbon deposits on Titan. *J. Geophys. Res. (Planets)* 115, 10005.
- Cornet, T. et al., 2012a. Geomorphological significance of Ontario Lacus on Titan: Integrated interpretation of Cassini VIMS, ISS and RADAR data and comparison with the Etosha Pan (Namibia). *Icarus* 218, 788–806.
- Cornet, T. et al., 2012b. Edge detection applied to Cassini images reveals no measurable displacement of Ontario Lacus' margin between 2005 and 2010. *J. Geophys. Res. (Planets)* 117, 7005.
- Griffith, C.A., Owen, T., Wagener, R., 1991. Titan's surface and troposphere, investigated with ground-based, near-infrared observations. *Icarus* 93, 362–378.
- Griffith, C.A. et al., 2005. The Evolution of Titan's mid-latitude clouds. *Science* 310, 474–477.
- Griffith, C.A. et al., 2012. Possible tropical lakes on Titan from observations of dark terrain. *Nature* 486, 237–239.
- Hayes, A. et al., 2008. Hydrocarbon lakes on Titan: Distribution and interaction with a porous regolith. *Geophys. Res. Lett.* 35, 9204.
- Hayes, A.G. et al., 2010. Bathymetry and absorptivity of Titan's Ontario Lacus. *J. Geophys. Res. (Planets)* 115, 9009.
- Hayes, A.G. et al., 2011. Transient surface liquid in Titan's polar regions from Cassini. *Icarus* 211, 655–671.
- Hayes, A.G. et al., 2013. Morphologic analysis of polar landscape evolution on Titan. *LPI Contrib.* 1719, 2000.
- Le Gall, A. et al., 2011. Cassini SAR, radiometry, scatterometry and altimetry observations of Titan's dune fields. *Icarus* 213, 608–624.
- Le Gall, A. et al., 2012. Latitudinal and altitudinal controls of Titan's dune field morphometry. *Icarus* 217, 231–242.
- Le Mouélic, S. et al., 2012. Global mapping of Titan's surface using an empirical processing method for the atmospheric and photometric correction of Cassini/VIMS images. *Planet. Space Sci.* 73, 178–190.
- Lockwood, G.W. et al., 1986. The albedo of Titan. *Astrophys. J.* 303, 511–520.
- Lorenz, R.D., 1994. Crater lakes on Titan: rings, horseshoes and bullseyes. *Planet. Space Sci.* 42, 1–4.
- Lorenz, R.D., Radebaugh, J., 2009. Global pattern of Titan's dunes: Radar survey from the Cassini prime mission. *Geophys. Res. Lett.* 36, 3202.
- Lorenz, R.D. et al., 2006. The sand seas of Titan: Cassini RADAR observations of longitudinal dunes. *Science* 312, 724–727.
- Lorenz, R.D. et al., 2008. Titan's inventory of organic surface materials. *Geophys. Res. Lett.* 35, 2206.
- Lorenz, R.D. et al., 2013. A global topographic map of Titan. *Icarus* 225, 367–377.
- Mastrogiuseppe, M. et al., 2014. The bathymetry of a Titan sea. *Geophys. Res. Lett.* 41, 1432–1437.
- McCord, T.B. et al., 2008. Titan's surface: Search for spectral diversity and composition using the Cassini VIMS investigation. *Icarus* 194, 212–242.
- McKay, C.P. et al., 1989. The thermal structure of Triton's atmosphere - Pre-Voyager models. *Geophys. Res. Lett.* 16, 973–976.
- Mitri, G. et al., 2007. Hydrocarbon lakes on Titan. *Icarus* 186, 385–394.
- Podolak, M. et al., 1984. Inhomogeneous models of Titan's aerosol distribution. *Icarus* 57, 72–82.
- Pollack, J.B. et al., 1980. On the relationship between secular brightness changes of Titan and solar variability. *Geophys. Res. Lett.* 7, 829–832.
- Radebaugh, J. et al., 2008. Dunes on Titan observed by Cassini radar. *Icarus* 194, 690–703.
- Rages, K., Pollack, J.B., 1980. Titan aerosols - Optical properties and vertical distribution. *Icarus* 41, 119–130.
- Rannou, P. et al., 1995. Titan's geometric albedo: Role of the fractal structure of the aerosols. *Icarus* 118, 355–372.
- Rodriguez, S. et al., 2006. Cassini/VIMS hyperspectral observations of the HUYGENS landing site on Titan. *Planet. Space Sci.* 54, 1510–1523.
- Rodriguez, S. et al., 2009. Global circulation as the main source of cloud activity on Titan. *Nature* 459, 678–682.
- Rodriguez, S. et al., 2011. Titan's cloud seasonal activity from winter to spring with Cassini/VIMS. *Icarus* 216, 89–110.
- Rodriguez, S. et al., 2014. Global mapping and characterization of Titan's dune fields with Cassini: Correlation between RADAR and VIMS observations. *Icarus* 230, 168–179.
- Roe, H.G. et al., 2005. Geographic control of Titan's mid-latitude clouds. *Science* 310, 477–479.
- Soderblom, L. et al., 2007. Correlations between Cassini VIMS spectra and RADAR SAR images: Implications for Titan's surface composition and the character of the Huygens Probe Landing Site. *Planet. Space Sci.* 55, 2025–2036.
- Soderblom, J.M. et al., 2012. Modeling specular reflections from hydrocarbon lakes on Titan. *Icarus* 220, 744–751.
- Sotin, C. et al., 2012. Observations of Titan's northern lakes at 5 μ m: Implications for the organic cycle and geology. *Icarus* 221, 768–786.
- Stephan, K. et al., 2010. Specular reflection on Titan: Liquids in Kraken Mare. *Geophys. Res. Lett.* 37, 7104.
- Stofan, E.R. et al., 2007. The lakes of Titan. *Nature* 445, 61–64.
- Tan, S.P., Kargel, J.S., Marion, G.M., 2013. Titan's atmosphere and surface liquid: New calculation using statistical associating fluid theory. *Icarus* 222, 53–72.
- Tokano, T., 2009. Impact of seas/lakes on polar meteorology of Titan: Simulation by a coupled GCM-Sea model. *Icarus* 204, 619–636.
- Tomasko, M.G. et al., 2008. A model of Titan's aerosols based on measurements made inside the atmosphere. *Planet. Space Sci.* 56, 669–707.
- Turtle, E.P. et al., 2009. Cassini imaging of Titan's high-latitude lakes, clouds, and south-polar surface changes. *Geophys. Res. Lett.* 36, L02204.
- Turtle, E.P. et al., 2011a. Seasonal changes in Titan's meteorology. *Geophys. Res. Lett.* 38, 3203.
- Turtle, E.P. et al., 2011b. Rapid and extensive surface changes near Titan's equator: Evidence of april showers. *Science* 331, 1414–1417.
- Vincendon, M., Langevin, Y., 2010. A spherical Monte-Carlo model of aerosols: Validation and first applications to Mars and Titan. *Icarus* 207, 923–931.
- Wall, S. et al., 2010. Active shoreline of Ontario Lacus, Titan: A morphological study of the lake and its surroundings. *Geophys. Res. Lett.* 37, 5202.